Linear-to-Circular Cross-Polarization Differential Detection for Atomic Co-Magnetometers Based on Polarization-Multiplexed Metasurfaces

Kun Huang[a,b,c,d,e], Xu Xiao[a,b,c,d,e], Zhibo Cui[a,b,c,d,e], Liangsong Pei[a,b,c,d,e], Zhen Chai[a,b,c,d,e,*]

a Key Laboratory of Ultra-Weak Magnetic Field Measurement Technology, Ministry of Education, School of Instrumentation and Optoelectronic Engineering, Beihang University, Beijing, 100191, China

b Institute of Large-scale Scientific Facility and Centre for Zero Magnetic Field Science, Beihang University, Beijing, 100191, China

c Hangzhou Institute of Extremely-Weak Magnetic Field Major National Science and Technology Infrastructure, Hangzhou, 370051, China

d Beihang Hangzhou Innovation Institute, Hangzhou, 310052, China

e Hefei National Laboratory, Hefei, 230088, China

E-mail: zhenchai@buaa.edu.cn

Supplement Information

Table 1. Comparison between the proposed metasurface-based detection and conventional bulk optics methods.

	Conventional Bulk Optics[1-3]	Existing Metasurfaces[4-7]	This work
System Profile	Millimeter to Centimeter	Micrometer	Micrometer
Component Count	Multiple	Single-layer device	Single-layer device
Polarization Mode	Hybrid (via multiple components)	Homogeneous (LP/LP or CP/CP)	Hybrid (LP + CP simultaneously)
Integration	Low	High	Ultra-high
Alignment	High	Low	Low
Interface Losses	Cumulative	Moderate	Low
Stability	Sensitive to vibration/drift	Robust	Robust
Scalability	Limited (Manual assembly)	High (CMOS-compatible)	High (CMOS-compatible)

Table 2. Quantitative comparison between the proposed work and state-of-the-art (SOTA) atomic detection systems.

	Sensitivity	Polarization Mode	Power Consumption
Zhu[8]	$\sim 10^{-8}$ rad	Hybrid (via discrete pieces)	High
Cui[9]	1.48×10^{-7}rad	Single (Homogeneous)	Moderate
Xu[5]	3.0526×10^{-5}rad	Single (Homogeneous)	Moderate
This work	5.9184×10^{-6}rad	Hybrid (LP & CP Integrated)	Low

SI.I：Phase shift and transmission amplitude of the rectangular meta-atoms as a function of the length Lx and width Ly

Conventional optical devices typically manipulate beam propagation or wavefront shaping through gradual phase accumulation during light transmission. This paradigm shifted when Capasso's team pioneered the use of phase-gradient metasurfaces for beam control. The foundation of arbitrary beam manipulation lies in satisfying the laws of refraction and reflection. However, since metasurfaces deviate from classical refraction/reflection laws, Capasso *et al.* introduced the generalized Snell's law to explain anomalous refraction and reflection phenomena, expressed as[10, 11]:

$$k_0 n_i \sin\theta_i \mathrm{d}x + (\varphi + \mathrm{d}\varphi) = k_0 n_t \sin\theta_t \mathrm{d}x + \varphi \qquad \text{(S1)}$$

where $k_0 = 2\pi/\lambda_0$ is the free-space wave vector, and λ_0 is the wavelength of the incident light. The first term on both sides of the equation represents the phase accumulated by light propagating along the path, and the second term represents the phase delay induced at the medium interface. Further simplification of the above equation yields the generalized Snell's law of refraction:

$$n_t \sin\theta_t - n_i \sin\theta_i = \frac{\lambda_0}{2\pi}\frac{\mathrm{d}\varphi}{\mathrm{d}x} \qquad \text{(S2)}$$

where $\mathrm{d}\varphi/\mathrm{d}x$ is the phase gradient carried by the metasurface.

Therefore, with a predetermined incident angle, arbitrary refraction angles can be achieved by engineering an appropriate phase gradient into the metasurface. Herein, we construct the metasurface by matching the designed birefringent phase profile with the phase and transmission response of rectangular meta-atoms. These meta-atoms comprise silicon nanorods arranged in a square lattice with fixed height (500 nm) and periodicity (388 nm) in air, whose optical properties were computed via finite-difference time-domain (FDTD) simulations. Fig. S1 demonstrates the phase modulation and transmission characteristics of the silicon square-lattice structures under varying transverse dimensions (Lx and Ly). By strategically tuning the nanorod geometry, the meta-atoms achieve full 2π phase coverage while maintaining high transmission efficiency.

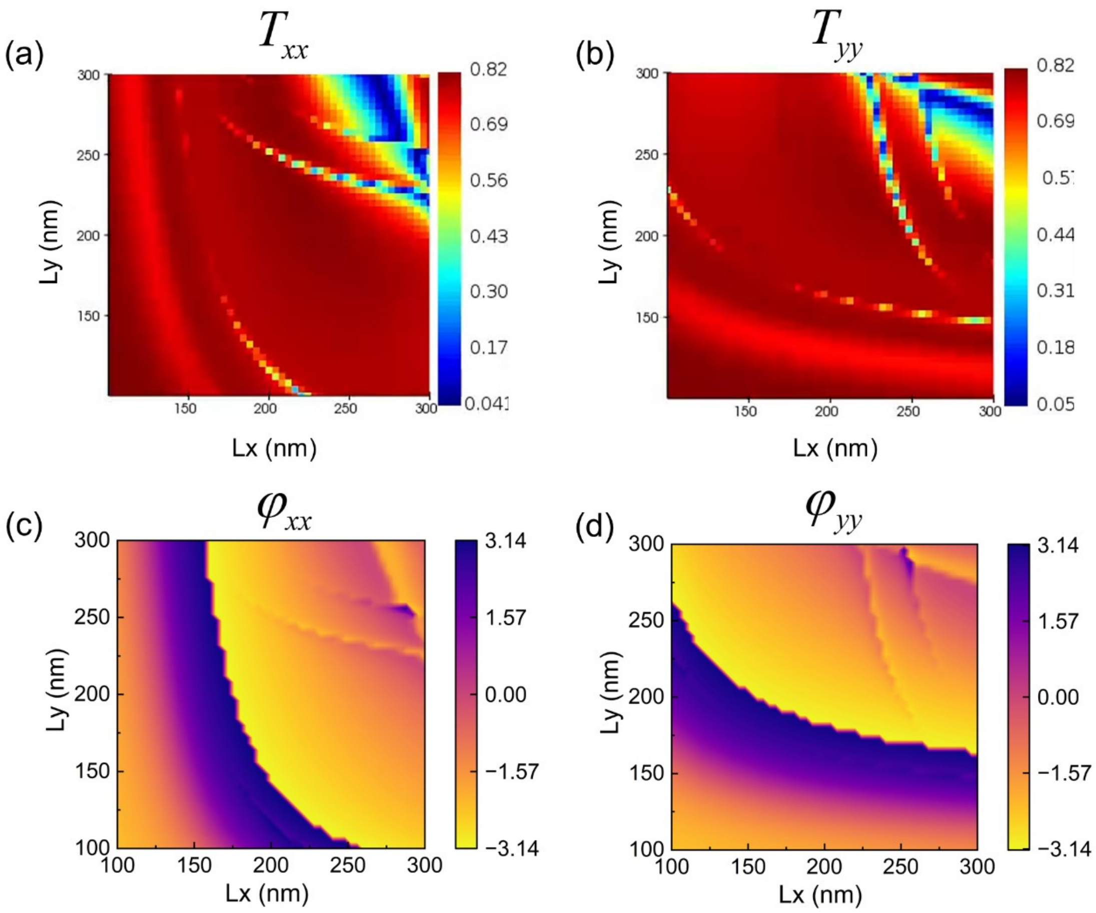

Fig. S1. Calculated transmission and phase shift of an incident x- or y- polarized plane wave, based on full-wave simulation of a square silicon array of rectangular rods with fixed lattice constant (P = 388 nm), pillar height (h = 500 nm), and swept transverse dimensions Lx and Ly.

SI.II：Calculated transmission coefficients and amplitude ratio of the polarization-multiplexed metasurface design being fabricated in this work

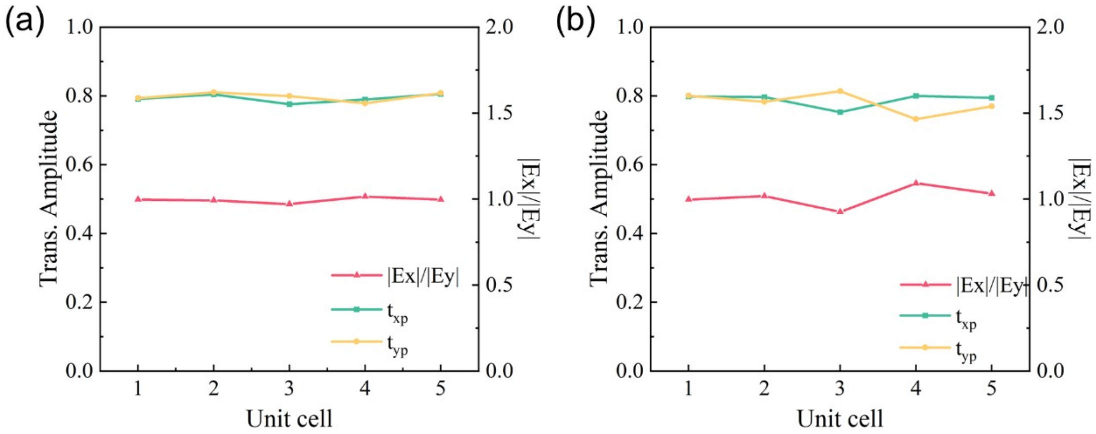

Fig. S2. Transmission amplitudes and amplitude ratio for PRD (a) and PCD (b) under 45° linearly polarized light incidence.

SI.III：Far-field electric field simulations and ellipticity analysis of representative meta-atom in polarization-multiplexed metasurfaces

To verify the functionality of individual meta-atoms within our polarization-splitting metasurface design, we characterized the transmitted light via ellipticity χ analysis. When p-polarized linear light (incident at $\psi = 45$ °) illuminates the meta-atom, the ellipticity is defined as[12]:

$$\chi = \frac{2\left|t_{\mathrm{xp}}\right|\left|t_{\mathrm{yp}}\right|\sin\left(\varphi_{\mathrm{xp}} - \varphi_{\mathrm{yp}}\right)}{t_{\mathrm{xp}}^{2} + t_{\mathrm{yp}}^{2}} \tag{S3}$$

Where t_{xp} and t_{yp} denote the transmission amplitudes along x- and y-directions, while φ_{xp} and φ_{yp} represent the corresponding transmission phases. Here, $\chi = 1$ and $\chi = -1$ correspond to perfect right-handed (RCP) and left-handed circularly polarized (LCP) light, respectively. It can be observed that, within the wavelength range of 700 nm to 900 nm, when the incident light is at an angle of 45° with respect to the x-axis, the ellipticity of the transmitted light through the meta-atoms in the PRD structure is close to 0. This indicates that the polarization state of the LP light remains unchanged after incidence on our designed meta-atoms (as shown in Figure S3b). In addition, the ellipticity of the transmitted light through the meta-atoms in the PCD structure is close to 1, implying that the LP light is converted into nearly perfect RCP light after incidence on our designed meta-atoms. Figure S3d shows the ellipticity of the transmitted light under different incident angles. It can be seen that when the incident light is at 45° or -45° with respect to the x-axis, the transmitted light is RCP light or LCP light, respectively.

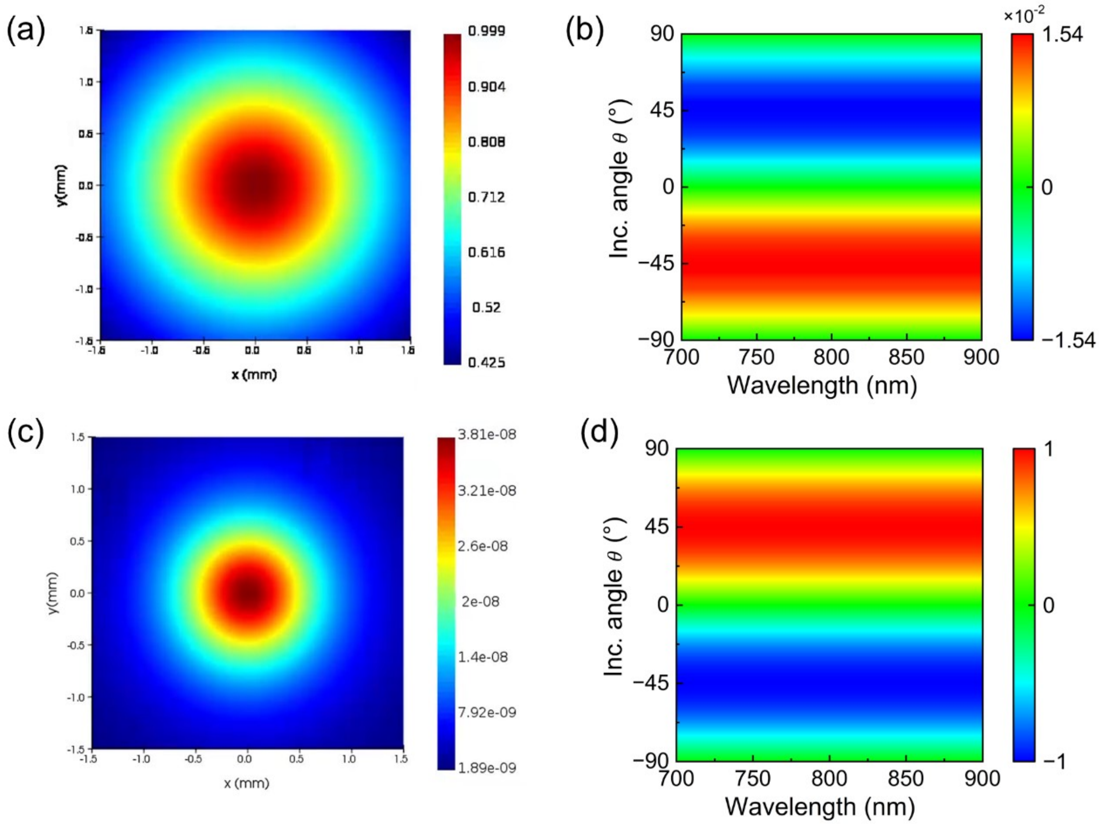

Fig. S3. Simulated far-field electric field (a) and ellipticity variation with incident polarization angle (b) for a selected unit cell (Lx = 180 nm, Ly = 192 nm) of the PRD. Similarly, corresponding simulations for a unit cell (Lx = 232 nm, Ly = 180 nm) of the PCD are shown in (c) and (d).

SI.IV Simulation calculations of far-field electric field profiles and polarization states for the polarization-multiplexed metasurface

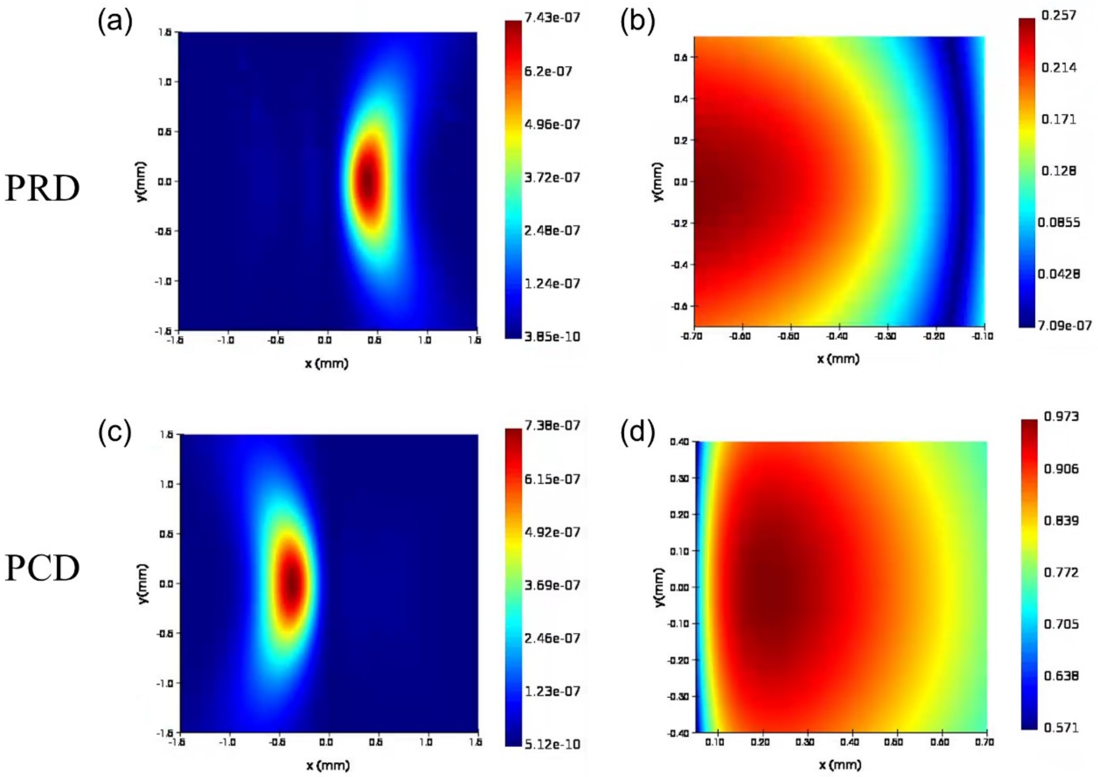

Fig. S4. Simulated far-field electric field profiles (a) and polarization states (b) for the PRD. Similarly, corresponding simulations for the PCD are shown in (c) and (d).

SI.V Schematic diagram of the detailed sample fabrication process

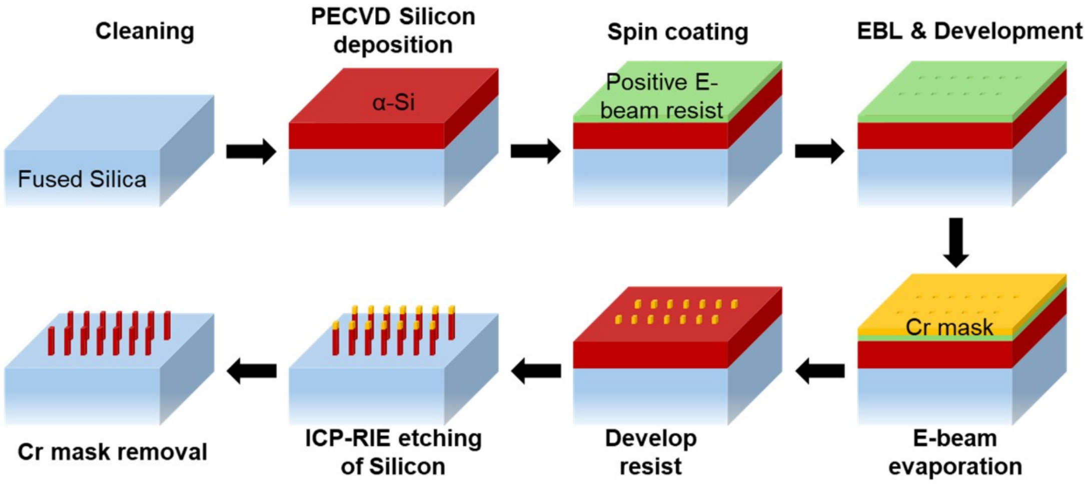

Fig. S5. Schematic diagram of the fabrication process flow.

SI.VI Spatial phase distributions transmitted through the PRD and PCD under 45° linearly polarized incidence, considering a 10 nm etching depth deviation.

Figure S6 illustrates the device's sensitivity to fabrication tolerances. When considering an etching depth deficiency of 10 nm, the transmitted spatial phase under 45° linearly polarized incidence exhibits a continuity that aligns well with the original design. This demonstrates that the device performance is robust against such etching depth variations.

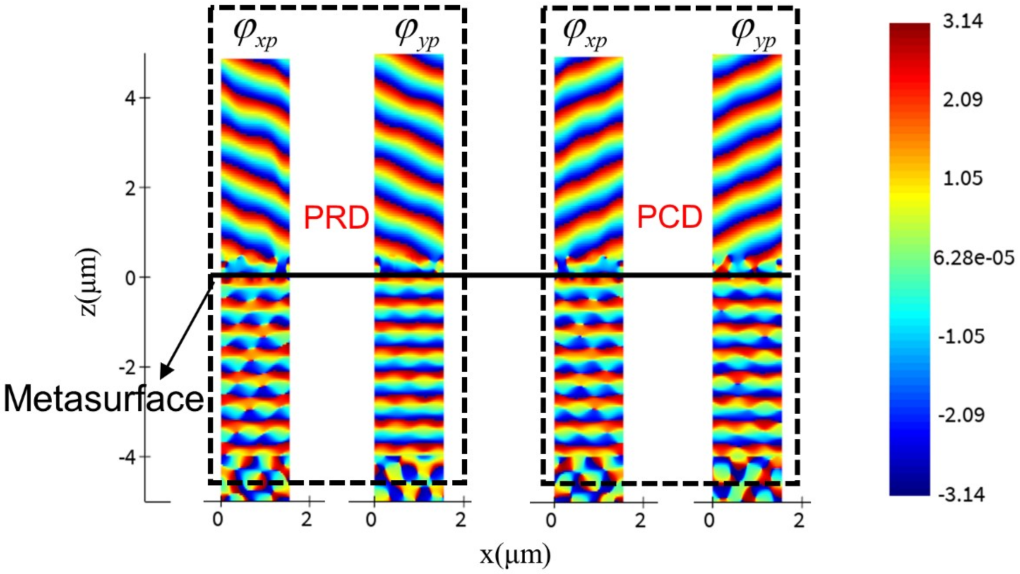

Fig. S6. Spatial phase profiles transmitted through the PRD and PCD under 45° linearly polarized incidence, considering a 10 nm etching depth error.

SI.VII Spatial phase distributions transmitted through the PRD and PCD under 45° linearly polarized incidence, considering a 5° sidewall tilt error.

The influence of a fabrication-induced 5° sidewall tilt is analyzed in Fig.S7. Under 45° linearly polarized incidence, the spatial phase distribution shows some degradation in continuity relative to the theoretical design. Despite these variations, the overall beam deflection is clearly discernible and remains consistent with the design goals, demonstrating the robustness of the device's primary function.

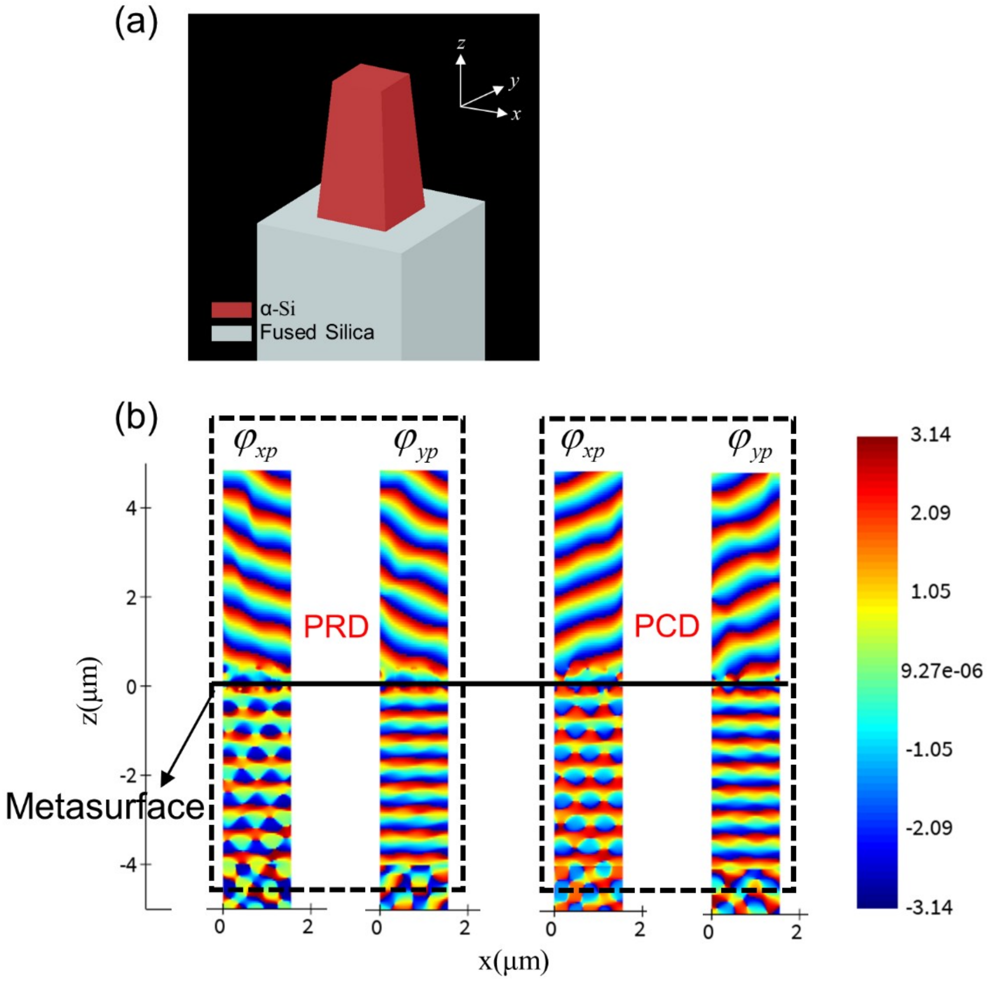

Fig. S7. Impact of a 5° sidewall tilt on the spatial phase profiles of the PRD and PCD. The incident light is 45° linearly polarized.

SI.VIII Transmitted spatial phase distributions of PRD and PCD under 45° linearly polarized incidence, considering a 10 nm etching depth deviation and 5° sidewall tilt.

We further considered the combined effect of etching depth errors and sidewall tilting under extreme fabrication scenarios. Upon illumination with 45° linearly polarized light, the resulting spatial phase profiles show a slight degradation in continuity; however, the global beam deflection is not significantly compromised. These results demonstrate that the device exhibits sufficient tolerance to fabrication errors to serve as a practical functional component.

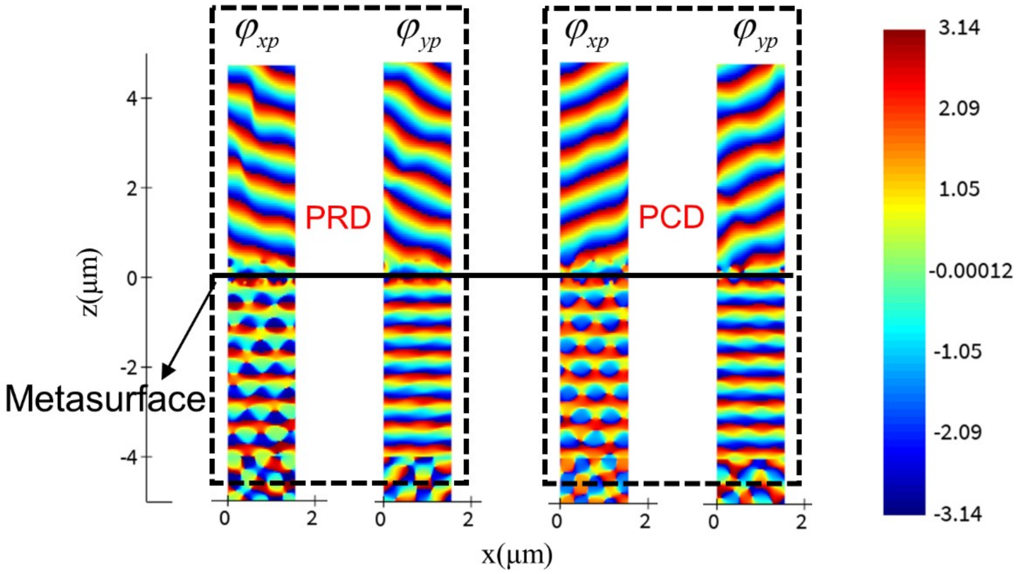

Fig. S8. Impact of extreme fabrication errors on the transmitted spatial phase profiles of the PRD and PCD.The results are obtained for a 10 nm etching depth deviation and 5° sidewall tilt with 45° linearly polarized incident light.

SI.IX Calculation of polarization states at different polarization angles when passing through the polarization-multiplexed metasurface under different incident angles

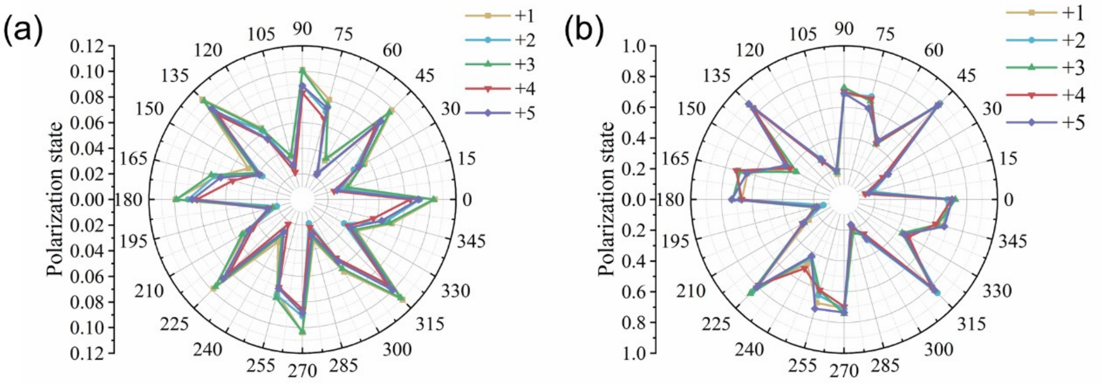

Fig. S9. Relationship between the polarization state of the emerging light after transmission through the PRD (a) and PCD (b) and the incident linear polarization angle, under various incidence angles. Polarization state values of 0 and 1 represent linear and circular polarization, respectively.

SI.X Diffraction efficiency of the polarization-multiplexed metasurface

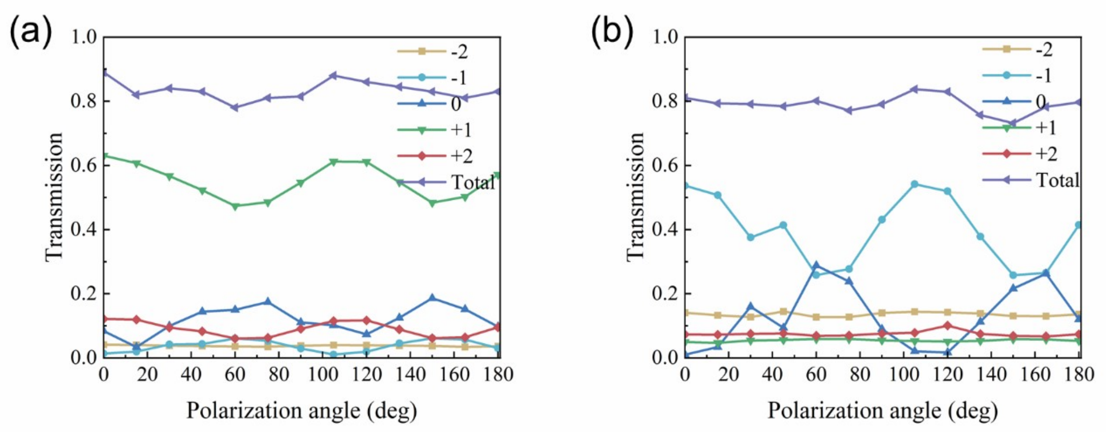

Fig. S10. Diffraction efficiencies for various orders under different incident linear polarization angles, corresponding to the PRD (a) and PCD (b).

SI.XI Experimental Setup for Angular Resolution Measurement Using Polarization-Multiplexed Metasurfaces

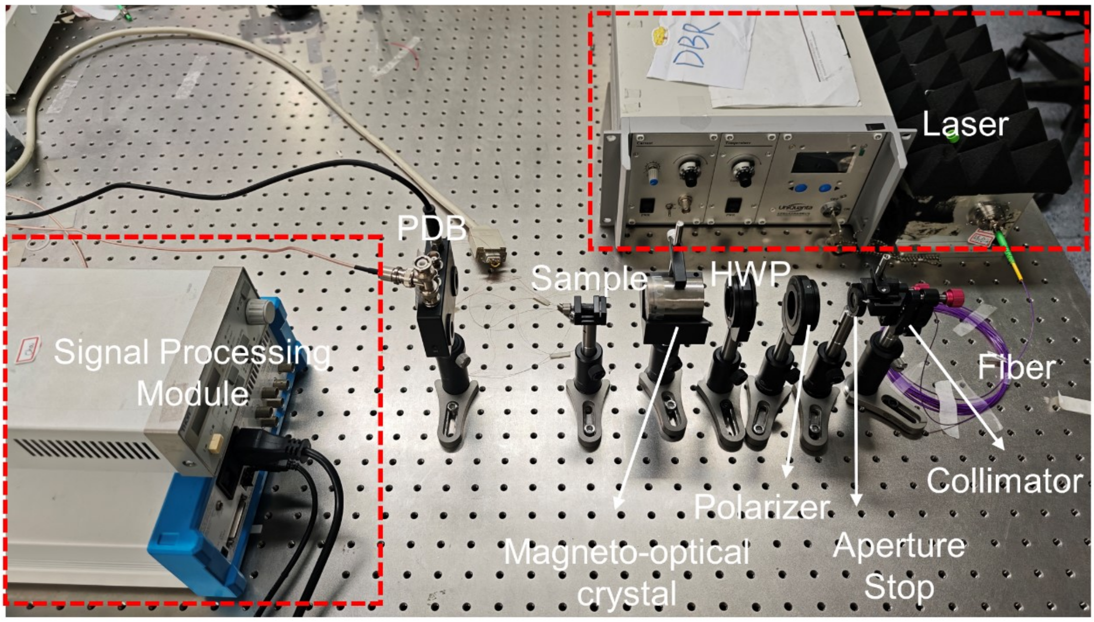

Figure S11. Experimental setup for measuring angular resolution using the polarization-multiplexed metasurface.

SI.XII PSD Estimation of Differentially Detected Signals via Periodogram

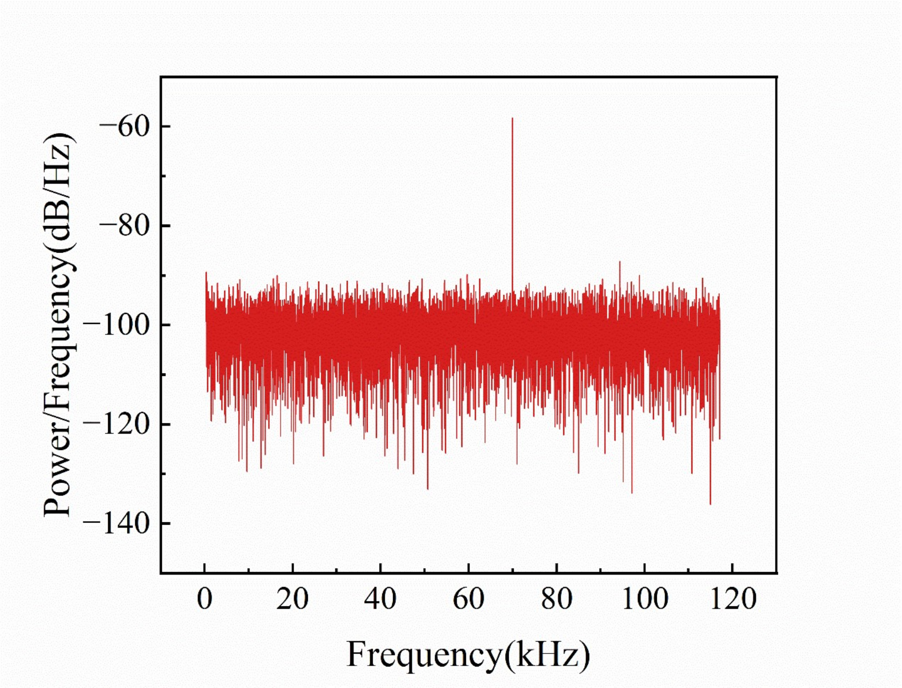

Fig. S12 Periodogram power spectral density estimate of the differential detection signal.

Reference

1. Y. Ma, *et al.*, Single-beam integrated hybrid optical pumping spin exchange relaxation free magnetometer for biomedical applications, *Appl. Phys. Lett.*, 2022, **121**, 114001.
2. G. Oelsner, *et al.*, Integrated optically pumped magnetometer for measurements within earth's magnetic field, *Phys. Rev. Appl.*, 2022, **17**, 024034.
3. Z. Yuan, *et al.*, Compact multi-channel optically pumped magnetometer for bio-magnetic field imaging, *Opt. Laser Technol.*, 2023, **164**, 109534.
4. J. S. Hu, *et al.*, Integrated optical rotation detection scheme for chip-scale atomic magnetometer empowered by silicon-rich SiNx metalens, *Opt. Lett.*, 2024, **49**, 3364-3367.
5. Y. Xu, *et al.*, Atomic spin detection method based on spin-selective beam-splitting metasurface, *Adv. Opt. Mater.*, 2024, **12**, 2301353.
6. X. T. Yang, *et al.*, Analysis of atomic magnetometry using metasurface optics for balanced polarimetry, *Opt. Express*, 2023, **31**, 13436-13446.
7. X. T. Yang, *et al.*, Atomic magnetometry using a metasurface polarizing beamsplitter in silicon-on-sapphire, *ACS Photonics*, 2024, **11**, 3644-3651.
8. R. Zhu, *et al.*, A compact optically pumped potassium atomic magnetometer with high sensitivity under geomagnetic field intensity, *Measurement*, 2025, **250**, 117099.
9. Z. B. Cui, *et al.*, Ultra-compact and high-precision differential detection method based on liquid crystal polarization grating for miniature atomic magnetometer, *Nanophotonics*, 2024, **13**, 4255-4265.
10. F. Aieta, *et al.*, Aberration-free ultrathin flat lenses and axicons at telecom wavelengths based on plasmonic metasurfaces, *Nano Lett.*, 2012, **12**, 4932-4936.
11. N. F. Yu, *et al.*, Light propagation with phase discontinuities: Generalized laws of reflection and refraction, *Science*, 2011, **334**, 333-337.
12. F. D. Wang, *et al.*, Highly efficient polarization control based on all-dielectric metasurfaces, *IEEE Access*, 2022, **10**, 32172-32179.